

Iron(II) pillared-layer responsive Frameworks via “kagomé dual” (kgd)

Supramolecular Tessellations

Shufang Xue,^{ab} Liang Wang,^a Anil D. Naik,^b Julianna Oláh,^c Koen Robeyns,^b Aurelian Rotaru,^d Yunnan Guo^{*ab} and Yann Garcia^{*be}

Abstract

Supramolecular tessellation represents newly emerging powerful tool for constructing crystalline and quasicrystalline structural aesthetics with molecular polygons/planigons. In turn, expanding such 2-periodic tessellation as tectonic layer to 3-periodic architecture of frameworks, promise the sublimation from visual beauty for pure appreciation to sophisticated performance of porous materials for real application, enabling us to build macroscopic behavior at the molecular scale. With the above foresight, we introduce herein a new discovery that integrating supramolecular tessellation and pillared-layer strategy assembles supramolecular frameworks (SFs). The tectonic layers are based on rhombille tessellation of hydrogen-bondings between Fe^{II} molecular building blocks and interstitial water molecules, showing a rare kagomé dual (**kgd**) net. Under this strategy, we first observed that a new **zlg** 3D topology was born by pillaring with **kgd** layer. These SFs offer potential channel/voids for guests' respiration, inducing a reversible allosteric transformation from ligand substitution. The transformation alters significantly the spin state which was quantified by ⁵⁷Fe Mössbauer spectroscopy, NMR, magnetic dilution and DFT calculations. These compounds show magnetic and chromatic bistability (see TOC), providing a broad scope towards multifunctional frameworks *via* multifarious supramolecular tessellation.

a. Department of Chemistry, Key Laboratory of Surface & Interface Science of Polymer Materials of Zhejiang Province, Zhejiang Sci-Tech University, Hangzhou 310018, China. E-mail: yunnanguo@zstu.edu.cn;

b. Institute of Condensed Matter and Nanosciences, Molecular Chemistry, Materials and Catalysis (IMCN/MOST), Université catholique de Louvain, Place L. Pasteur 1, Louvain-la-Neuve 1348, Belgium. E-mail: yann.garcia@uclouvain.be;

c. Department of Inorganic and Analytical Chemistry Budapest University of Technology and Economics H-1111 Budapest, Gellért tér 4. Hungary;

d. Department of Electrical Engineering and Computer Science and MANSiD Research Center, “Stefan cel Mare” University, University Street, 13, Suceava 720229, Romania.

e. Lead Contact

† Electronic supplementary information (ESI) available. CCDC 2031041 and 2031042. For ESI and crystallographic data in CIF or other electronic format see DOI:

1. Introduction

Supramolecular frameworks (SF)¹, which are architected through coordination and covalent bonding of their corresponding building units, furnished by non-covalent interactions, have recently attracted significant attention as alternative porous materials. Compared with traditional metal organic frameworks (MOFs) and covalent organic frameworks (COFs), SFs are superior because of their facile synthesis using mild reaction conditions, easy purification, and regeneration by recrystallization.^{1,2} Especially, using metal coordination complexes as building blocks is promising to produce functional Supramolecular Metal Organic Frameworks (SMOFs),³ by virtue of the diverse redox, magnetic⁴ and catalytic⁵ properties of metal ions, bringing new horizons for gas adsorption, programmable luminescence, catalysis, and molecular recognition.⁵⁻⁷

Currently, one of the most representative strategy for synthesizing SFs is the pillared-layer structure,⁸ where 2D thick layers interdigitated structures can be obtained and then stabilized by weak interactions, such as H-bonding and π - π stacking. Both the void within the layers and the interlayer space could accommodate guest molecules. Such supramolecular porous frameworks are quite flexible, providing a good platform to study various structural transformations.

In pillared-layer strategy, the underlying layers can be isolated through deconstruction of the crystal structure, and *in fine*, designed and constructed from judiciously selected building units⁹. It is well known that, edge-transitive nets are ideal targets in crystal chemistry. To apply this to pillared-layer structures, it is important to recognize that there are only five edge-transitive 2-periodic nets that exist, **sql** (square lattice), **kgm** (Kagome´), **hcb** (honeycomb), **hex** (hexagonal lattice) and **kgd** (Kagome´ dual). This is what Eddaoudi et al. recently introduced in the supermolecular building layer approach with pillaring.¹⁰ Therefore, targeting these nets and their corresponding pillared versions can facilitate rational design of desired porous architectures. So far, the first four edge-transitive layers have been successfully pillared toward porous materials, while it has not yet been conquered with the **kgd** (Kagome´ dual) layer.

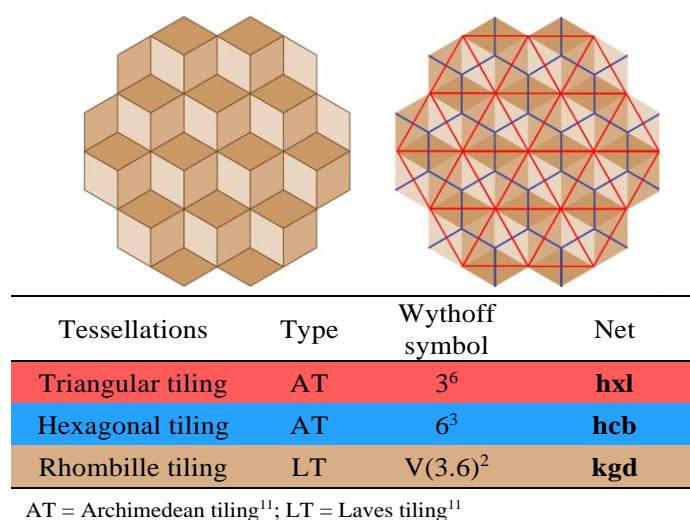
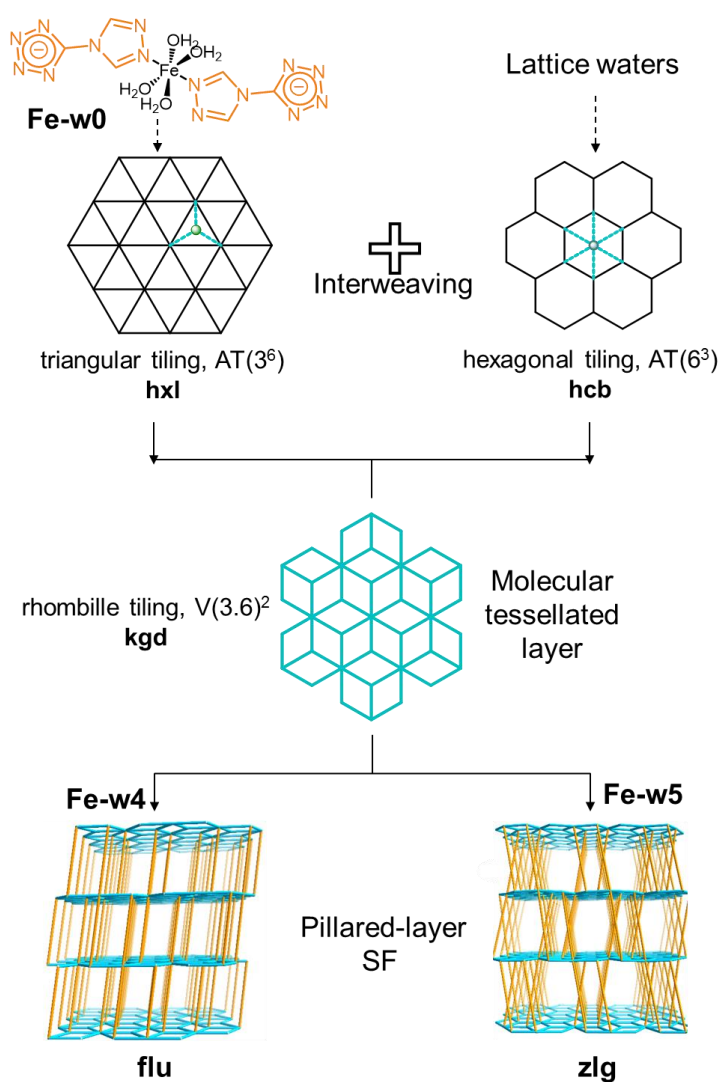


Figure 1. (Left) The rhombille tiling contains **kgd** net.¹² (Right) Two dual well-centred tessellations (the red edges of triangular tiling and blue edges of hexagonal tiling) generated from the diagonals of a rhombille tiling (shown by the light brown shading). The short diagonals of the rhombi form a set of hexagonal tiling; the long diagonals of the rhombi form another set of triangular tiling. Table below shows the representation of the corresponding tessellations.

The main reason is that, the **kgd** net (Figure 1 left) requires two different nodes: one being 3-c trigonal and the other one being hexagonal 6-c, making it extremely challenging to target and inherent difficult in pillaring.¹³ However, looking from the perspective of structural aesthetics, it became clear that **kgd** net can be achieved by supramolecular tessellations based on rhombille tiling (a tessellation of the plane by rhombi with 60° and 120° angles). Intriguingly, this can be generated by interweaving of two dual well-centred triangular tiling and hexagonal tiling (Figure 1 right).¹² In the past decade, great effort has been devoted to the development of regular, semi-regular and complex tilings on surfaces using self-assembly approaches¹⁴⁻¹⁶. Rhombille tiling as a Laves tiling, has been achieved in the field of 2D materials. For example, Wang *et al.*¹⁷ reported a 2D surface covalent rhombille tiling based on the Schiff base reaction between C6 symmetry and amine monomer with C3 symmetry. One might ask whether rhombille tessellation could be pillared to more complex SF architecture, to overcome the nature of being difficult to pillar with **kgd** layer.



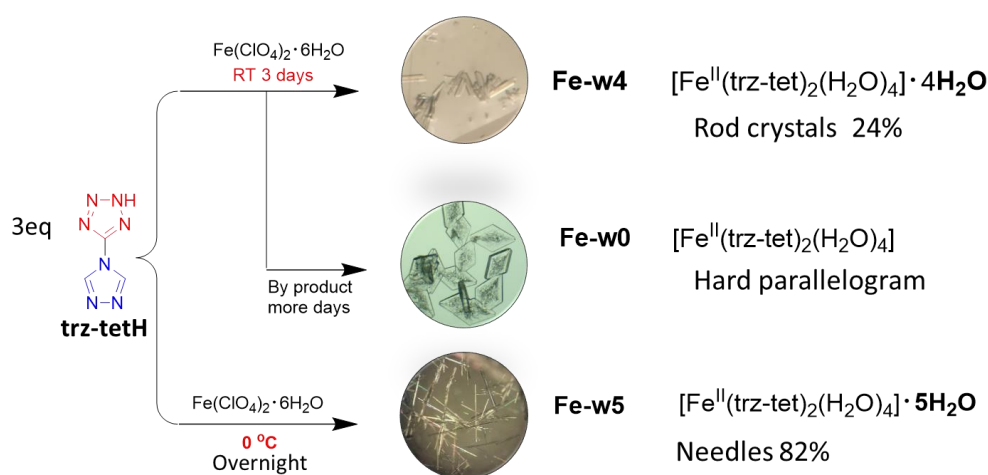
Scheme 1. Topological design of supramolecular rhombille tiling (**kgd**) via **Fe-w0** molecules and lattice waters, leading to pillared layer SFs of **Fe-w4** and **Fe-w5**, being **flu** and newly **zlg** nets, respectively.

With the above questions, we introduce herein a new discovery that integrates supramolecular tiling and pillared-layer strategy to assemble SF platforms. An Fe^{II} molecule ([Fe(**trz-tet**)₂(H₂O)₄], **Fe-w0**) was developed in two new pillared-layer SFs by combining lattice water, namely [Fe(**trz-tet**)₂(H₂O)₄]·4H₂O, (**Fe-w4**) and [Fe(**trz-tet**)₂(H₂O)₄]·5H₂O, (**Fe-w5**), with **trz-tetH** = 5-(4H-1,2,4-triazol-yl)-2H-tetrazole) (Scheme 1). There into, their **kgd** layers were constructed by rhombille tiling, which can be regarded as the interweaving of supramolecular tessellations between triangular tiling of **Fe-w0** and hexagonal tiling of lattice waters. Especially, under this strategy, we first observed that a new **zlg** 3D topology was born by pillaring with **kgd** layer in **Fe-w5**. These SFs offer potential water channel/voids for alcohol sensing *via* a spin state change (here in MeOH). More impressively, they are in total juxtaposition to what observed in its solvatomorph **Fe-w0**, which did not possess interstitial water with tight packing of Fe^{II} functional molecules, and consequently locked the guests' respiration channel for further sensing process. Therefore, this finding provides fascinating opportunities for creating vapor/solvent responsive magnetic materials,¹⁸⁻²¹ based on a simple but constructional supramolecular synthon.

2. Synthesis and crystallization

2.1 Synthesis and molecular structures

Scheme 2 summarizes the reactions carried out between **trz-tetH** and Fe^{II} at variable temperature for crystallization. Initially, slow evaporation takes place in water at room temperature to give colourless rod crystals (**Fe-w4**).²² Nevertheless, this method shows a relative low yield of 24%. En route to grabbing more materials of **Fe-w4** by increasing the evaporation time, parallelogram crystals without sensing properties were formed, which were identified as a by-product (**Fe-w0**). Therefore, as the production of the sensor materials is concerned, we decreased the temperature, in order to promote the yield. Surprisingly, this method allowed us to isolate a new SF [Fe(**trz-tet**)₂(H₂O)₄]·5H₂O (**Fe-w5**) as needle crystals. The structures of **Fe-w0**, **Fe-w4** and **Fe-w5** were refined in the monoclinic *C2/c*, triclinic *P-1* and monoclinic *P2₁/n* space groups, respectively. Details of the structure refinement and data acquisition are collected in Table S1 in the Supporting Information. The reader is referred to Table S2 for the values of selected bond lengths and bond angles described in the following.



Scheme 2. Summary of the reactions carried out between **trz-tetH** and Fe(ClO₄)₂·6H₂O with different conditions.

As shown in Figure 2, crystals of **Fe-w0**, **Fe-w4** and **Fe-w5** are solvatomorphs and contain a common chemical unit, namely, $[\text{Fe}(\text{trz-tet})_2(\text{H}_2\text{O})_4]$, in which all of the Fe^{II} atoms are located in a FeN_2O_4 environment, conferring a slightly distorted octahedral coordination (Table S 2). The equatorial planes are formed by four coordinated water O atoms, while the axial positions are occupied by two triazole N atoms of two **trz-tet** ligands. Thereinto, **trz-tet** acts as an anionic ligand with deprotonation of the labile proton on the tetrazole moiety **trz-tetH**.

Except **Fe-w0** which is solvent free, both **Fe-w4** and **Fe-w5** contain different stoichiometric ratio of lattice water. In **Fe-w4**, there are two independent interstitial water (O14 and O15), and half mononuclear Fe^{II} molecule in the asymmetric unit.²² Therefore, the stoichiometric ratio between the complex and lattice water becomes 1:4, as Fe^{II} is on a crystallographic inversion centre. However, **Fe-w5** contains five stoichiometric interstitial water molecules yielding a formula $[\text{Fe}(\text{trz-tet})_2(\text{H}_2\text{O})_4] \cdot 5\text{H}_2\text{O}$.

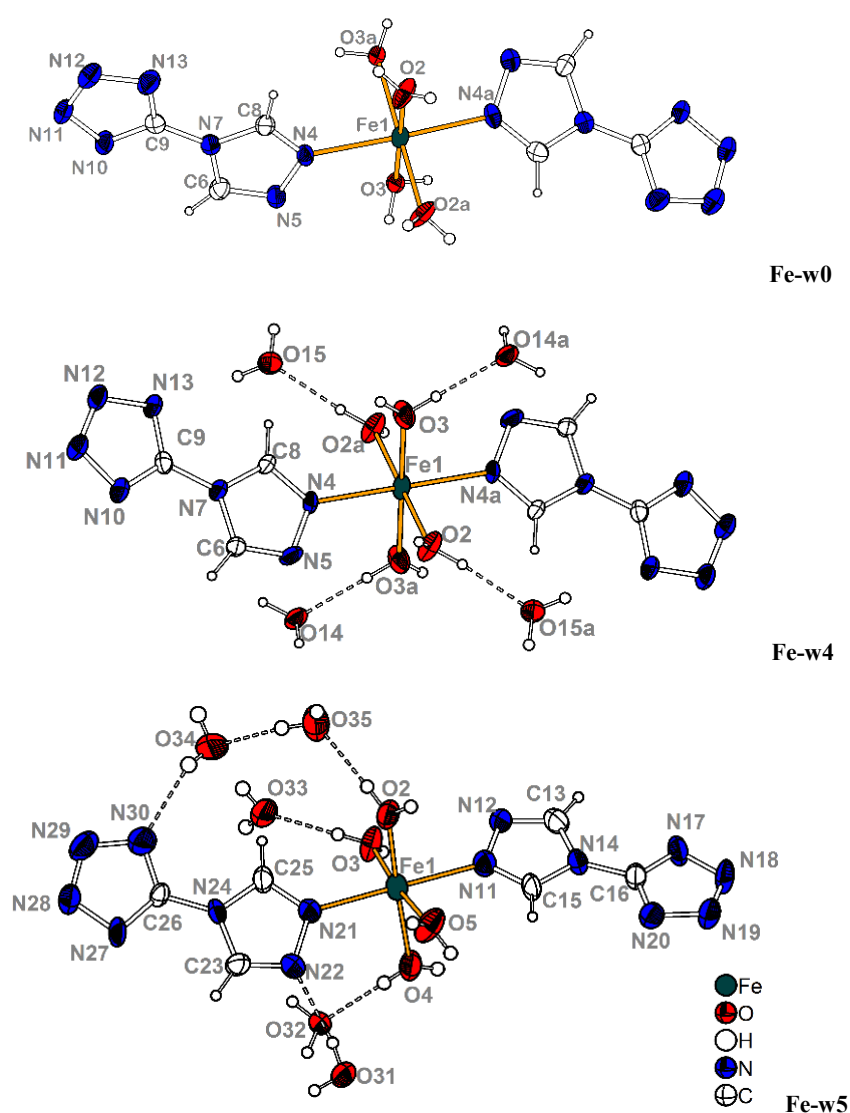


Figure 2. Atom labelling and crystal structure with 80% probability thermal ellipsoids: (top) **Fe-w0**, with symmetry code a: $-x, y, 0.5-z$; (middle) **Fe-w4**, with symmetry code a: $1-x, 1-y, 2-z$; and (bottom) **Fe-w5**.

2.2 Fe-w5 and Fe-w4: who is who?

Because of the similarity of appearance based on colour and shape between **Fe-w4** and **Fe-w5**, their essence may be wrongly believed as the same structure (Scheme 2). To ensure the uniformity of **Fe-w4** and **Fe-w5**, the powder X-ray diffraction (PXRD) patterns were measured at room temperature (Figure 3a). The peak positions of the simulated (Mercury Software) and as-synthesized PXRD for complexes **Fe-w4** and **Fe-w5** are in good agreement with each other, suggesting good phase purity of the complexes. It is reasonable to discriminate **Fe-w4** and **Fe-w5** by the fingerprint of the distinguishable peaks at low angle diffraction, especially, centred at 8.66° from (0 0 1) plane of **Fe-w4** and 7.90° from (0 0 2) plane of **Fe-w5**, noticed in Figure 3a ($F_{001} = 0$ because of systematic extinction for $P2_1/n$).

Simultaneously, the stoichiometric interstitial water in **Fe-w5** can be further identified by TGA curves (Figure 3b), which were performed on freshly prepared material of a single crystal sample. Care was required to start the experiments immediately upon loading the samples, as the dry nitrogen purge alone was sufficient to induce dehydration at ambient temperatures. The profile of **Fe-w5** shows a similar two-step mass loss with **Fe-w4**, corresponding to the lattice water molecules (r.t.- 98°C); and the coordinated water molecules (98 - 200°C). However, the larger weight change (18.73%) of first step in **Fe-w5** is in fair agreement with formula of five water molecule per Fe^{II} unit (cal. 18.4%).

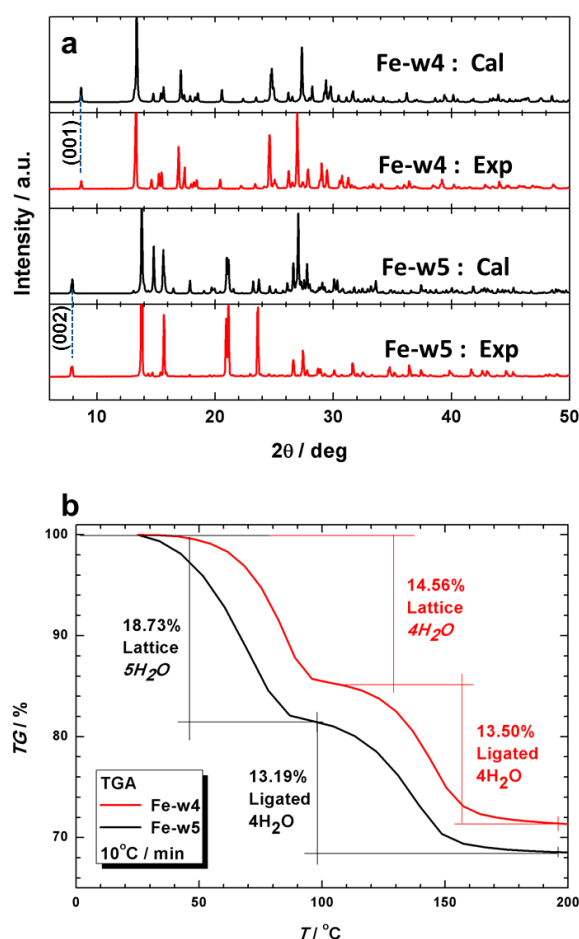


Figure 3. Identification different crystals of **Fe-w4** and **Fe-w5** by (a) Simulated (black lines) and as-synthesized (red lines) PXRD patterns; (b) TGA profile.

3. Supramolecular Analysis

The supramolecular behaviour of **Fe-w0**, **Fe-w4** and **Fe-w5** is mainly characterized by a dense 3D hydrogen bond (HB) network adopted among the Fe^{II} molecules and lattice waters. However, the existence or nonexistence of interstitial water directly affects their supramolecular structure, consequently, accompanying distinct differences of the performance on sensing properties (*vide infra*).

3.1 Supramolecular structure of *Fe-w0*

The structure of **Fe-w0** can be considered (Figure 4a, left) as a 2D triangular tiling propagate in *ab* plane. This arrangement can be viewed as geometric expressions of regular Archimedean tilings AT (3⁶), where molecule centres are placed at the vertices of the polygons (Figure 4a, right), with the Fe⋯Fe separation of 6.0747(3) and 6.3269(6) Å. In this plane, each molecule interacts *via* HB interactions with its six neighbouring molecules (Figure 4b), involving O2-H2A⋯O3 from the coordinated water and O3-H3B⋯N5 interaction based on triazolite cycles (Table S3). These layers (Figure 5a) are further connected by adjacent layers of tetrazole N11 and N12 as the acceptors, which run along the crystallographic *c*-axis, demonstrating the ultimate 3D supramolecular network shown in Figure 5b.

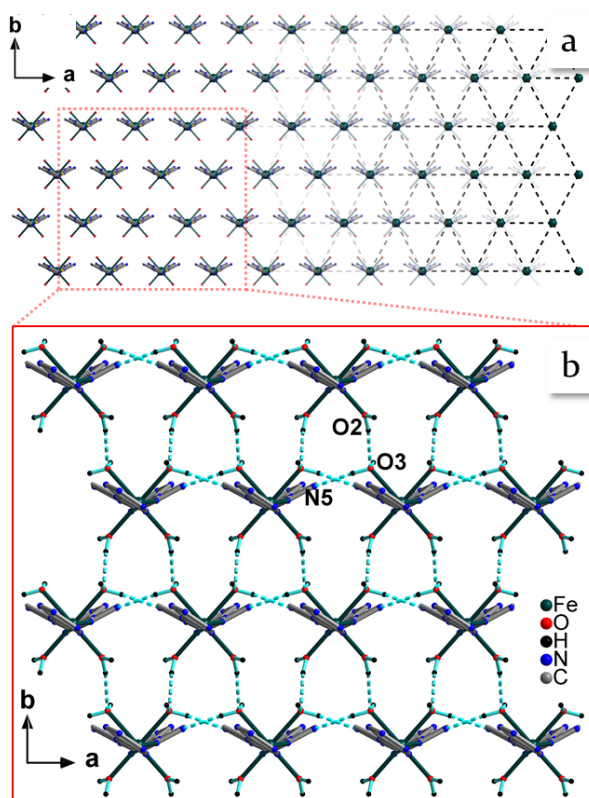


Figure 4. (a) Triangular tiling **Fe-w0** in the *ab*-plane. (b) HBs propagating of the discrete mononuclear entities within triangular tiling.

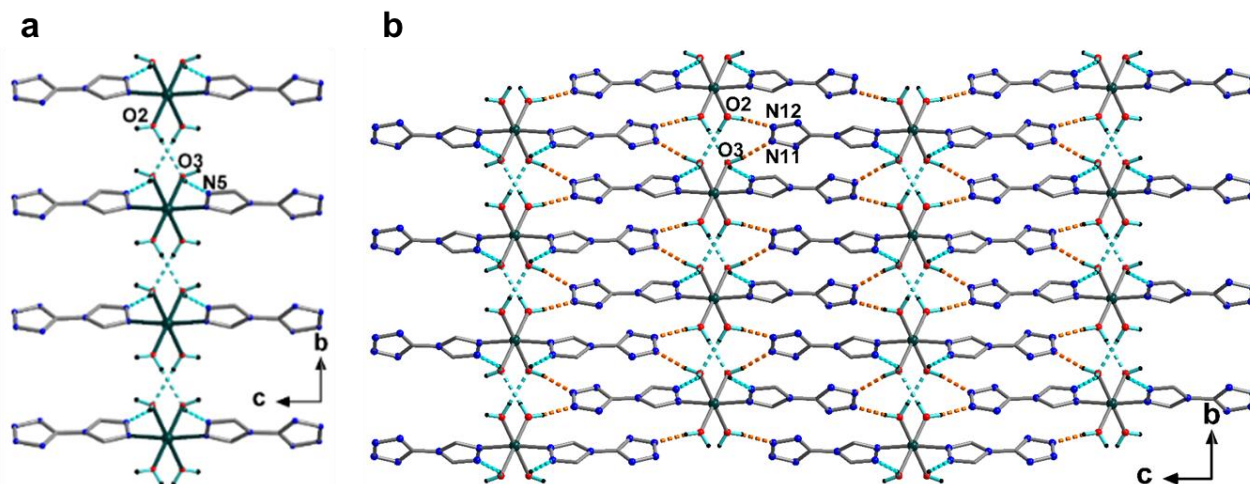


Figure 5. (a) lateral view of HBs along ab -plane in **Fe-w0**. (b) 3D supramolecular crystal packing of **Fe-w0**, in which HBs propagating along $[0\ 0\ 1]$ are coloured orange dash lines. For clarity, hydrogen atoms of C-H are omitted. HBs are depicted with cyan dash lines.

Furthermore, the 3D arrangement also implies two strands of π - π stacking from **trz-tet** ligand along $[-1\ 1\ 0]$ and $[1\ 1\ 0]$ (Figure S1a, b), in which the triazole rings and tetrazole rings form anti-parallel face-to-face assembly [distances between the tetrazole ring and the triazole ring alternatively 3.386 and 3.359 Å, (Figure S2)], keeping the inversion centre symmetry of the space group. Because every $\text{Fe}(\text{trz-tet})_2(\text{H}_2\text{O})_4$ unit connects four adjacent units by π - π interactions in different directions, which can be abstracted as a four-connected node (Figure S2), **Fe-w0** is featured as a 3D diamond-like π - π stacking network (Figure S1c). The abundant hydrogen bonds and tight π - π interactions resulting in closer packing lead **Fe-w0** to have a higher density compared to **Fe-w4** and **Fe-w5**, which is agreement with the hard nature of crystals.

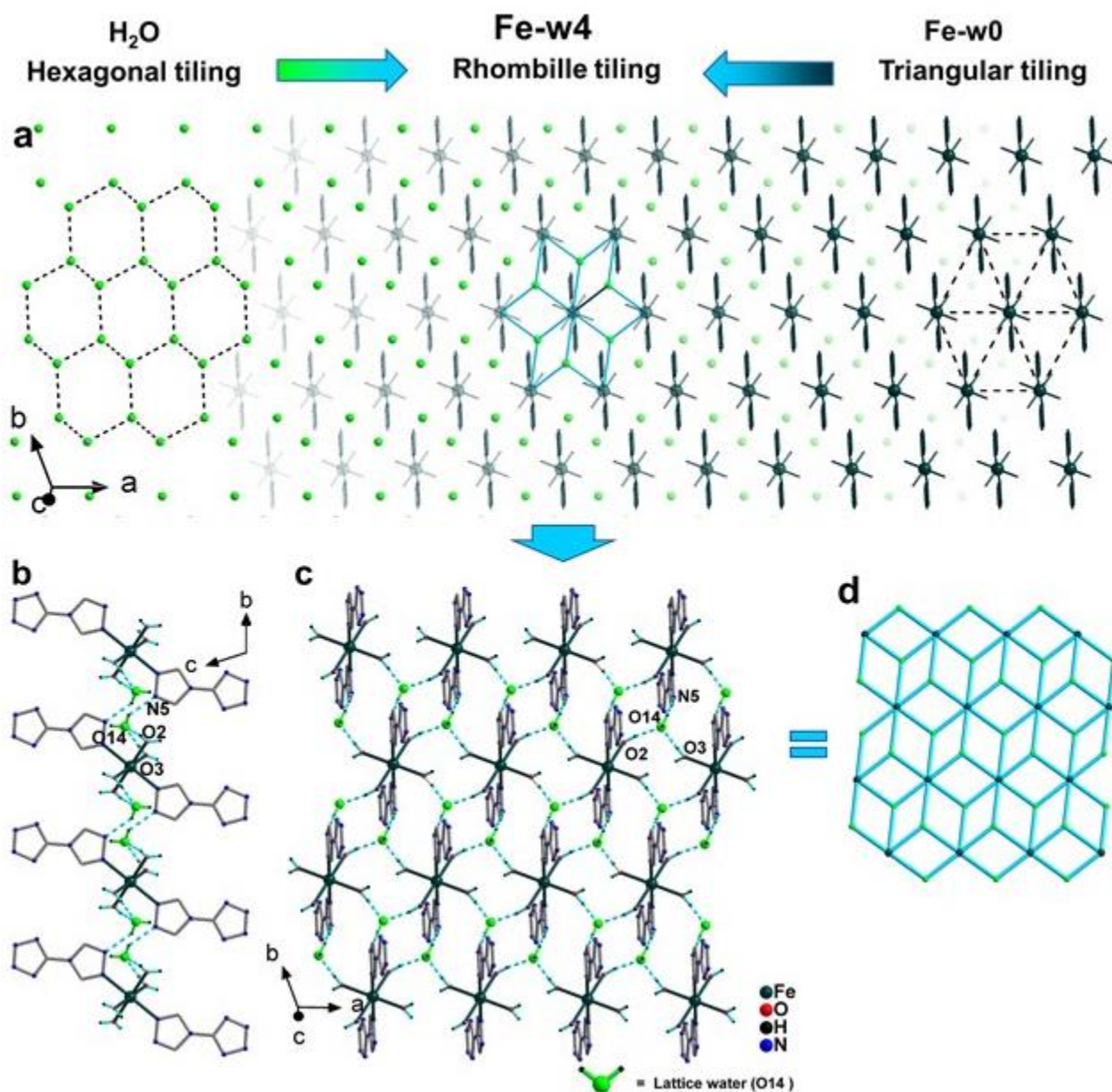


Figure 6. Supramolecular tessellations of Rhombille tiling in ab plane of **Fe-w4**. (a) Rhombille tiling formation based on the interweaving between the hexagonal tiling of lattice water ($\text{H}_2\text{O14}$) and triangular tiling of $\text{Fe}(\text{trz-tet})_2(\text{H}_2\text{O})_4$ molecules; A lateral view (b) and perpendicular view (c) of HBs propagating in rhombille tiling. Lattice waters $\text{H}_2\text{O14}$ is presented in green colour and the resulting HB are depicted with cyan dashed lines. (d) displaying the **kgd** 2D topology in rhombille tiling.

3.2 Tessellations of *Fe-w0* with lattice water

By contrast, molecular arrangement in **Fe-w4** was strongly changed by the existence of interstitial water. As observed in ab plane (Figure 6a), each **Fe-w0** molecule was surrounded by six lattice waters ($\text{H}_2\text{O14}$), in which, the hexagonal arrangement of $\text{H}_2\text{O14}$ can be viewed as geometric expressions of regular $\text{AT}(6^3)$ (Figure 6a, left), whereas the **Fe-w0** molecules keep their original arrangement pattern of triangular tiling [$\text{AT}(3^6)$] (Figure 6a, right). The $\text{Fe}\cdots\text{Fe}$ distances being 6.5493(11), 7.5664(19) and 8.0203(23) Å, are larger than those in the **Fe-w0** crystal. This supramolecular structure can be interpreted as interwoven tessellations of the two phases of $\text{AT}(6^3)$ and $\text{AT}(3^6)$, leading to the formation of new rhombille grid with $\text{H}_2\text{O14}$ and **Fe-**

w0 as the vertices (cyan lines overlain on the crystal structure images in Figure 6a). Further evidence for this impressive arrangement was indicated by the presence of the HB network. As shown in Figure 6b-c, HBs between **Fe-w0** and H₂O14 play the role of the edges of rhombille tiling [HBs: O2-H2A···O14, O3-H3A···O14 and O14-H14B···N5]. Therefore, as far as topological analysis is concerned, this rhombille tiling belongs to HB connected **kgd** topology, which is even rare in MOFs.²³

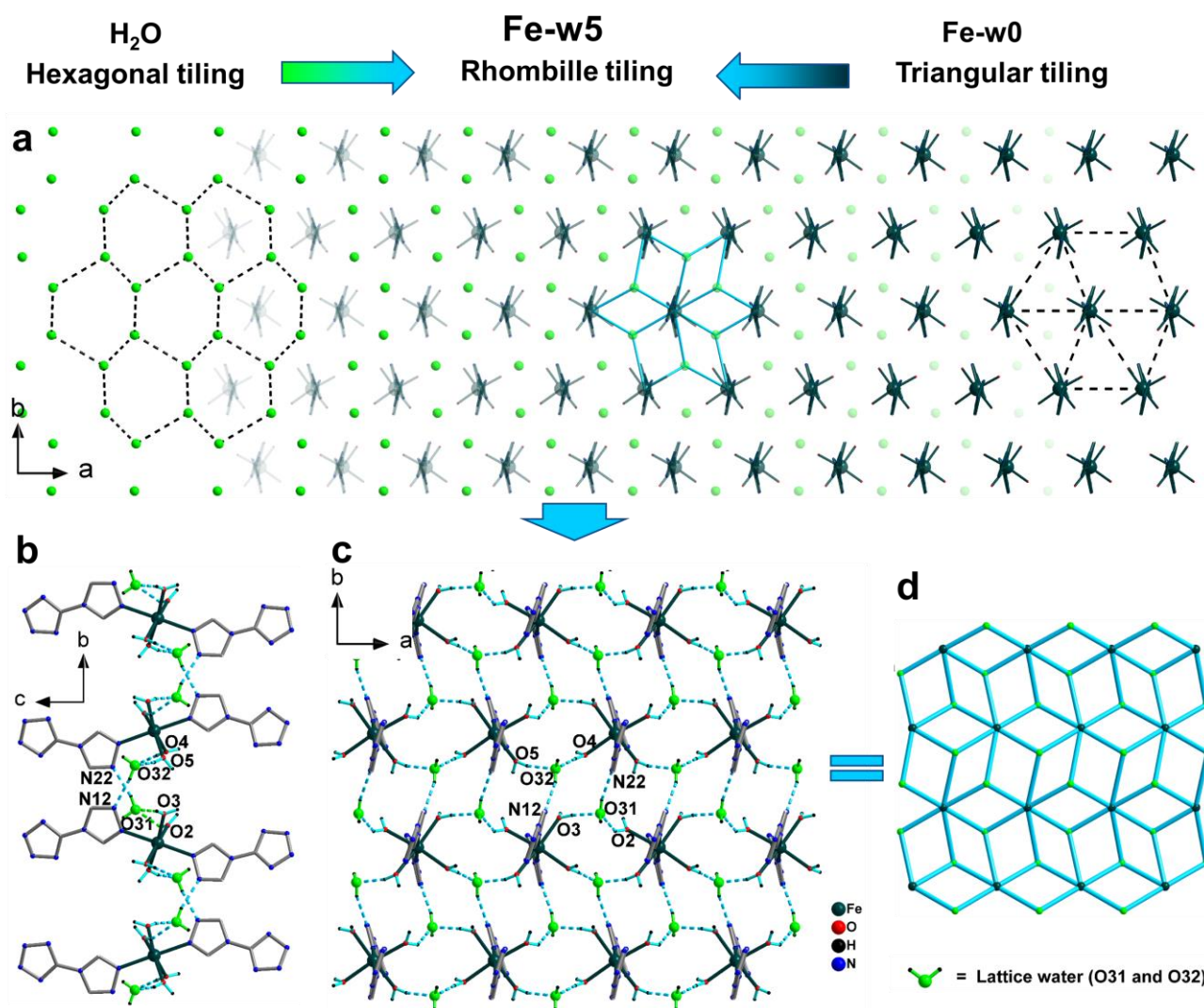


Figure 7. Supramolecular tessellations of Rhombille tiling in *ab* plane of **Fe-w5**. (a) Rhombille tiling formation based on the interweaving between the hexagonal tiling of lattice water (H₂O31 and H₂O32) and triangular tiling of Fe(**trz-tet**)₂(H₂O)₄ molecules; A lateral view (b) and perpendicular view (c) of HBs propagating in rhombille tiling. Lattice waters H₂O31 and H₂O32 is presented in green colour and the resulting HB are depicted with cyan dash lines. (d) displaying the **kgd** 2D topology in rhombille tiling.

Surprisingly, the packing arrangements of **Fe-w5** can also reproduce such rhombille supramolecular tessellation in its *ab* plane (Figure 7a). The overall tiling in a 2D plane derived from the propagation of HB interactions is shown in Figure 7b-c, where each H₂O31 and H₂O32 bridges three adjacent Fe^{II} molecules, [HBs: O2-H2B···O31, O3-H3B···O31 and O31-H31A···N22 from H₂O31; O4-H4A···O32, O5-H5A···O32 and O32-H32B···N12 from H₂O32]. Corresponding **kgd** net can also be successfully fabricated by using

H₂O as a linker, as shown in Figure 7d. Apparently, the tiling patterns in **Fe-w4** and **Fe-w5** crystal structure were absolutely different from the packing arrangements in the **Fe-w0**, demonstrating the significance of the introduction of solvents in crystallization conditions towards novel tessellations.²⁴

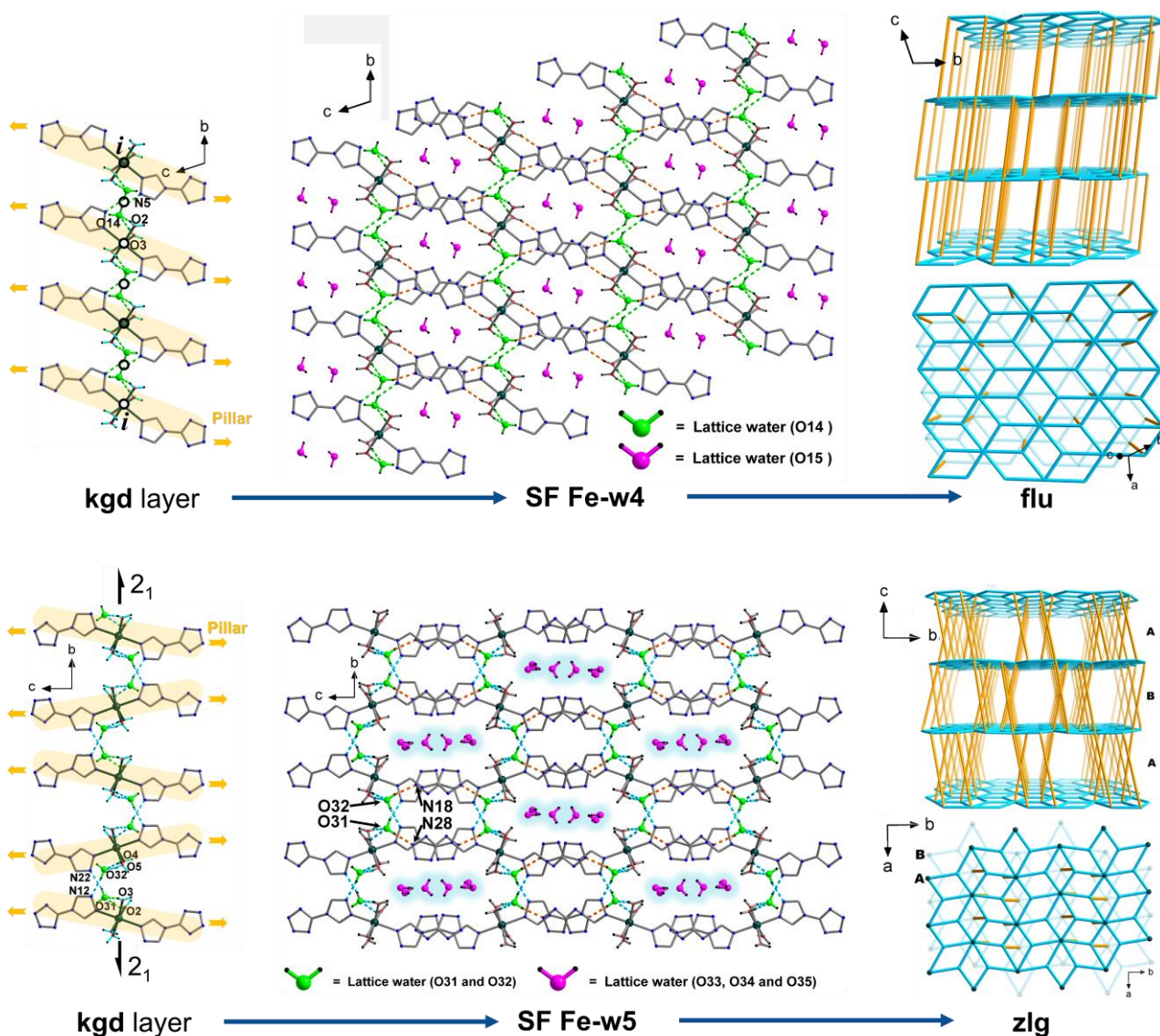


Figure 8. SF structures of **Fe-w4** (top) and **Fe-w5** (bottom). (left) lateral view of **kgd** layers highlighting of the pillar ligands with indicated symmetry operations; (middle) SF via pillaring supramolecular tessellations, looking down the [0 0 1] direction, emphasizing the channels/voids hosting interstitial water. (right) Schematic of the pillaring of **kgd** layers showing **flu** and **zlg** topologies.

3.3 SFs by pillaring of *kgd* layers.

trz-tet ligands are coordinated on two sides of the **kgd** layer, while the triazole heads show strong HB acceptor nature. Therefore, the layers are further pillared by HB in between triazole N and lattice water of adjacent layers to generate the 3D frameworks for both **Fe-w4** and **Fe-w5** (Figure 8). From a topological viewpoint, the **kgd** layers adding additional pillars can be regarded to be changed the original 6-c and 3-c in 2D to 8- and 4-connected nodes in 3D nets. As a result, as shown in Figure 8 (right), the structures of **Fe-w4**

and **Fe-w5** can be simplified as (4,8)-connected net with the point symbol of $\{4^{12}.6^{12}.8^4\{4^6_2$ (**flu**) and $\{4^{12}.6^{10}.8^6\{4^6_2$ (herein named **zlg**, Zhejiang LiGong University), respectively. **zlg** for **Fe-w5** topology is new and now added to the Reticular Chemistry Structure Resource (RCSR) database. By far, many (4,8)-connected MOFs have been reported, and most of them exhibit **flu**,^{25, 26} **scu**,²⁷ **sqc**,²⁸ **csq**²⁹ or **sjt**³⁰ topology. **Fe-w5** represent the first framework with **zlg** net topology.

The reason for their different 3D nets comes from the arrangement of pillar ligand relative to their **kgd** layers. In **Fe-w4**, the ligands coordinate to Fe^{II} ions with inversion centre symmetry (Figure 8, left), leading to parallel alignment each other forming common **flu** topology. Nevertheless, in **Fe-w5**, the arrangement of **trz-tet** adopt the operation of 2_1 screw axis along [0 1 0] direction located in **kgd** layers, causing the ligands tilting each other and the formation of novel **zlg** topology. This tilt effect in **Fe-w5** brings a relative large space to stock one more lattice water than **Fe-w4** (Figure S 4 and Figure S 5a), which leads to the formation of 1D channels running parallel to the [1 0 0] direction. Within the channels, the water molecules H₂O33 H₂O34 and H₂O35 are arranged in serpentine chains involved in HB connection one by one (Figure S5b). The channels correspond to 14.1% (279 Å³) of the unit cell volume (1982.5 Å³) (Figure S5c, calculated with CALC SQUEEZE instruction to calculate after removal of the water molecules).

The filling of interstitial water gravely weakened the stacking of ligands, forming a weak off-set $\pi \cdots \pi$ interactions. Finally, The Fe^{II} molecules have large gaps and are not tightly arranged, which eventually leads to a lower density. Interstitial water strongly modified the circumstances of Fe^{II} molecules, bringing **kgd** layer, pillared-layer SF, water channels/voids and weakened $\pi \cdots \pi$ stacking. These appearances contrast sharply with those observed in **Fe-w0** without interstitial water, which finally lead them to two dramatically different paths on the sensor performance (*vide infra*).

4. Allosteric sensing mechanism in Fe-w5

Given the colourimetric sensor behaviour of **Fe-w4** for alcohol series,³¹ the title complexes **Fe-w0** and **Fe-w5** were also subjected to vapor-phase detection with MeOH as the most sensitive analyte. **Fe-w0** is not capable of sensing MeOH, and can be regarded as an impurity of **Fe-w4**, which can be observed in SEM image (Figure S7a) and PXRD spectrum (Figure S7b and Figure S7c). Therein, **Fe-w0** as the impurity of **Fe-w4** exhibits inertia without any crystal form transformation during vapor diffusion.

4.1 Optical sensing properties in Fe-w5

UV-Vis diffuse reflectance spectroscopy (DRS) of **Fe-w5** (Figure 9) shows one broad band (Band I) in the near-IR region, between $\lambda = 700$ and 1100 nm and then no discernible feature until the absorption intensity increases sharply below $\lambda = 350$ nm, i.e., in the charge-transfer region. Band I originates from spin allowed $d-d$ transitions (${}^5T_{2g} \rightarrow {}^5E_g$ for HS d^6 in O_h symmetry). The spectrum is agreement with the colourless appearance of the crystals. When **Fe-w5** is exposed to vapor of MeOH(g), the crystals turn deep pink within hours. DRS shows λ_{\max} at 515 nm, and is accompanied by a broadened band from UV to 400 nm. We conducted a subtraction of the spectrum before and after sensing with MeOH, which represents the contributions of the new chromophore in the pink form, and which is characterized by double bands feature as shown Figure 9 for blue line, marked as (Bands II and III). Interestingly, this double bands nature can be regarded as the finger print of a d^6 low-spin (LS) system, as usually observed in electronic spectrum Fe^{II}³² and Co^{III} complexes³³, corresponding to spin-allowed $d-d$ transitions ${}^1A_{1g} \rightarrow {}^1T_{1g}$ and ${}^1A_{1g} \rightarrow {}^1T_{2g}$ (Tanabe-Sugano diagram was shown in Figure S11).

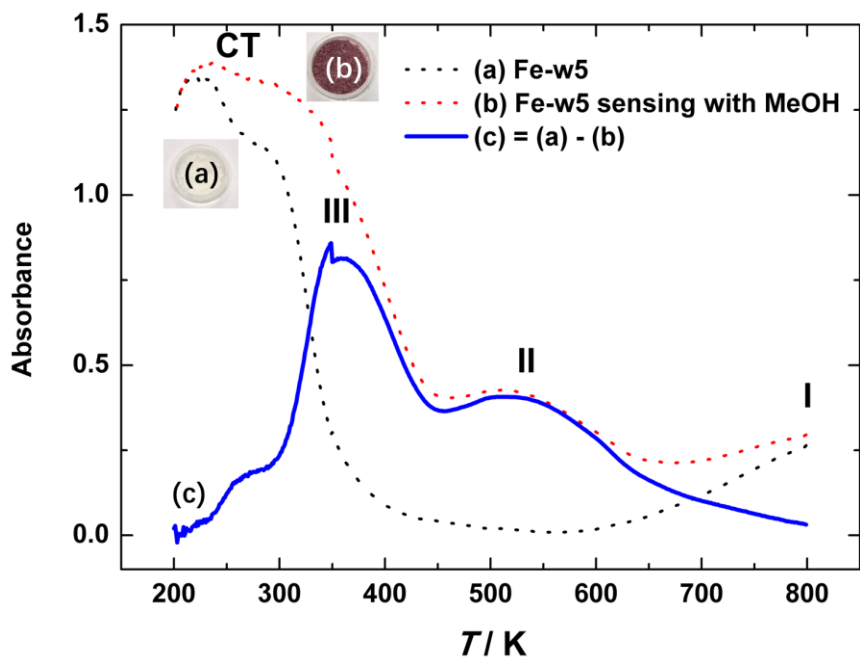


Figure 9. UV-Vis diffuse reflectance spectroscopy (DRS) of **Fe-w5** (a) before and (b) after MeOH exchange; (c) demonstrating of spin-allowed *d-d* transitions of FeN_6 species from the subtraction between (a) and (b).

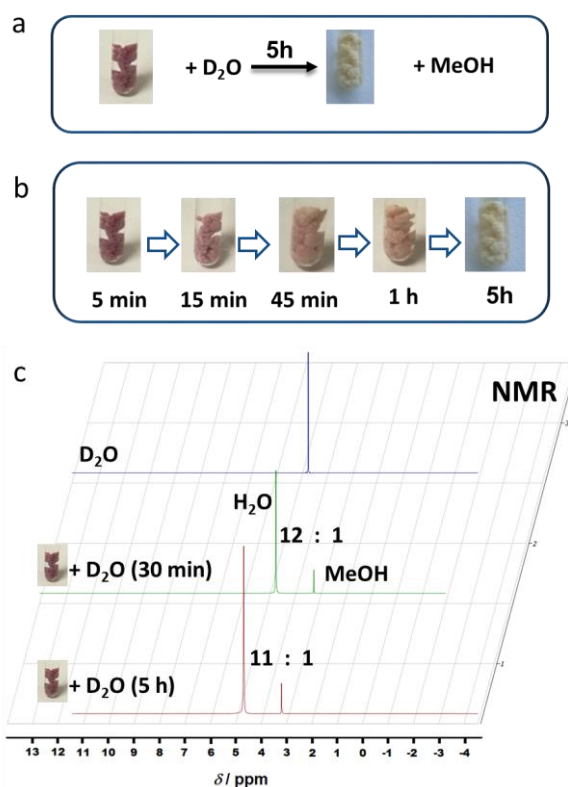


Figure 10. ^1H NMR investigation for the regeneration of colourimetric sensor with the pink sample, derived from the MeOH diffusion of **Fe-w5** over ca. 10 h. (a) the Regeneration from pink to colourless by soaking with deuterated water. (b) Real-time imaging of process of regeneration at room temperature. (c) ^1H NMR for D_2O with pink form at different regeneration times.

Collection of the crystal structure of pink form was not possible, because **Fe-w5** undergoes structure collapse to amorphous upon guest intrusion (Figure S8). Nevertheless, it exhibits a colour change from pink turning back to colourless as reversible process, when exposed to water vapor or soaked with water for regeneration (Figure 10a), while regenerating a crystalline phase (Figure S8). To delve into how H₂O molecules recover the FeN₂O₄ sphere as **Fe-w5**, we conducted proton nuclear magnetic resonance (¹H NMR) experiments with soaked pink sample in D₂O, derived from the MeOH diffusion of **Fe-w5** over ca. 10 h (Figure 10c). This process is manifested by a very fast leaching of MeOH within 30 min based on the signal of 3.34 ppm in D₂O, which is out of synchronization with the colour change (LS to high-spin (HS)) as shown in Figure 10b. Therefore, the reaction of pink LS-Fe^{II} chromophore with H₂O is rate limiting for the regeneration of sensor, reflecting by the optical band of $\lambda = 510$ nm disappearance (Figure S9).

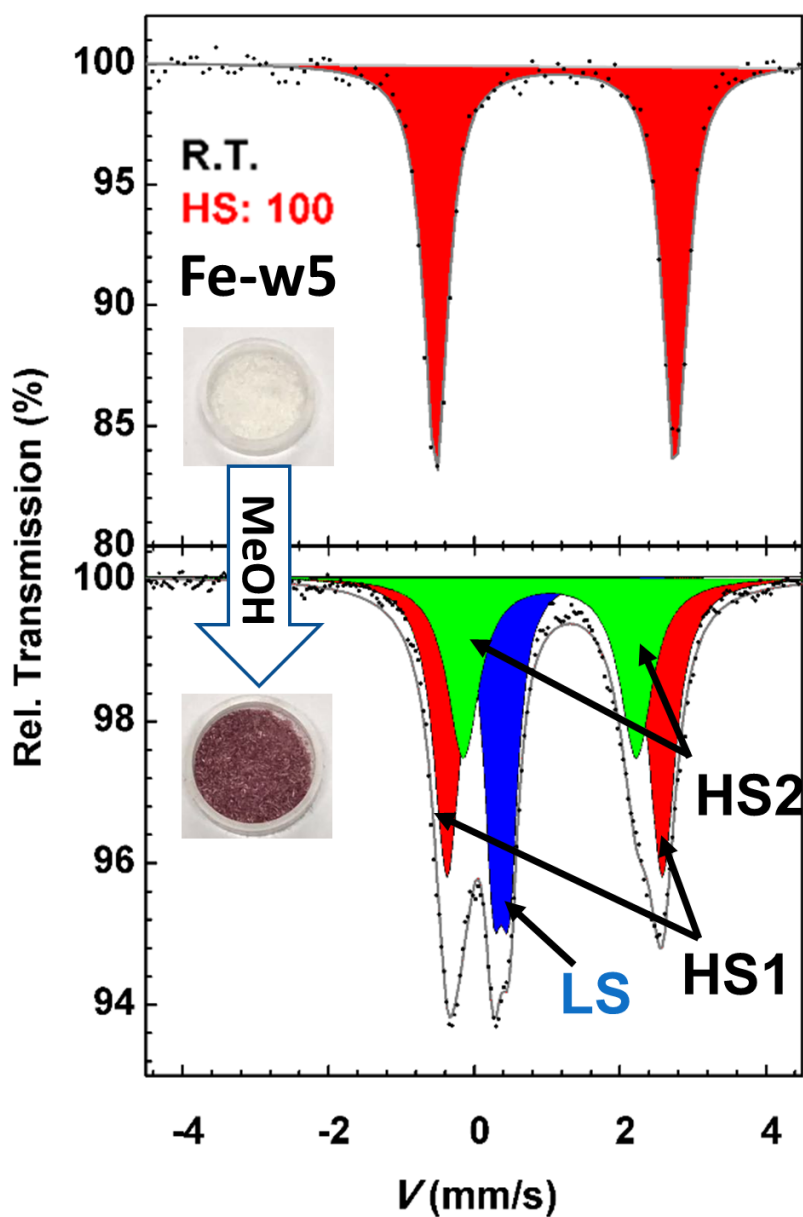


Figure 11. Spin-state tracking by ⁵⁷Fe Mossbauer spectroscopy at 298 K before and after MeOH exchange for **Fe-w5**, corresponding ⁵⁷Fe Mössbauer parameters listed in Table 1.

4.2 Essence of optical sensing in Fe-w5

^{57}Fe Mössbauer spectroscopy confirms the driving force of this colourimetric sensing behaviour (Figure 11), which is anticipated to be due to a spin-state switching of Fe^{II} centre. Initially, **Fe-w5** shows a unique doublet with an isomer shift $\delta = 1.17(2)$ mm/s and a quadrupole splitting $\Delta E_Q = 3.18(3)$ mm/s, in agreement with the HS FeN_2O_4 environment. After vapor diffusion by MeOH, the spectrum of pink sample made it possible to deconvolute and identify a significant spectral area of a new quadrupole doublet [$\delta = 0.37$ mm/s; $\Delta E_Q = 0.22$ mm/s, 26%], characteristic of a LS Fe site, coloured in blue in Figure 11, besides another two HS states HS1 and HS2. SQUID magnetometry also supports this observation by the 25% lower χ_{MT} value (Figure S10). Since the substitution of coordinated water molecules by MeOH still with FeN_2O_4 chromophore (Form **B** in Figure 12) is not expected to shift the ligand-field strength into the LS region, an allosteric mechanism is imperative. An uncoordinated tetrazole moiety of the neighbouring mononuclear unit is displaced from its mean position to be coordinated to iron, thus leading to a LS FeN_6 core (Form **C** in Figure 12). Actually, this FeN_6 LS has been observed with similar isomer shifts and quadrupole splittings in $[\text{Fe}_3(\text{trz-tet})_6(\text{H}_2\text{O})_6] \cdot 2\text{H}_2\text{O}$, and 1D coordination polymer $[\text{Fe}(\text{trz-tet})(\text{trz-tetH})_2]\text{BF}_4 \cdot 2\text{MeOH}$,³⁴ from the normal solution reaction. The most precious behaviour in **Fe-w5** is that the spin state change can be triggered by allosteric sensing in solid state.

Table 1. Spectroscopic assignments for **Fe-w5** before and after MeOH exchange.

	UV-vis	Mössbauer			Spin state	Crystal Field			
	λ_{max} [nm]	δ [mm/s]	ΔE_Q [mm/s]	pop. [%]		ΔO^a [cm ⁻¹]	ε^b [cm ⁻¹]		
Fe-w5	983	298K	1.17	3.18	100	HS	10173	805	FeN_2O_4 (H_2O)
	$^5T_{2g} \rightarrow ^5E_g$	77K	1.16	3.38					
Fe-w5 sensing with MeOH	972	298K	1.1	2.95	43	HS1	10288	689	FeN_2O_4 (MeOH)
	$^5T_{2g} \rightarrow ^5E_g$	77K	1.18	3.29					
	361	298K	1.04	2.37	31	HS2	10288	499	
	$^1A_{1g} \rightarrow ^1T_{2g}$	77K	0.93	3.07					
515	298K	0.37	0.22	26	LS	21235	Negligible	FeN_6	
$^1A_{1g} \rightarrow ^1T_{1g}$	77K	0.3	0.3						
$[\text{Fe}_3(\text{trz-tet})_6(\text{H}_2\text{O})_6] \cdot 2\text{H}_2\text{O}^c$		298K	0.40	0.15					FeN_6
$[\text{Fe}(\text{trz-tet})(\text{trz-tetH})_2]\text{BF}_4 \cdot 2\text{MeOH}^c$		298K	0.35	0.18					FeN_6

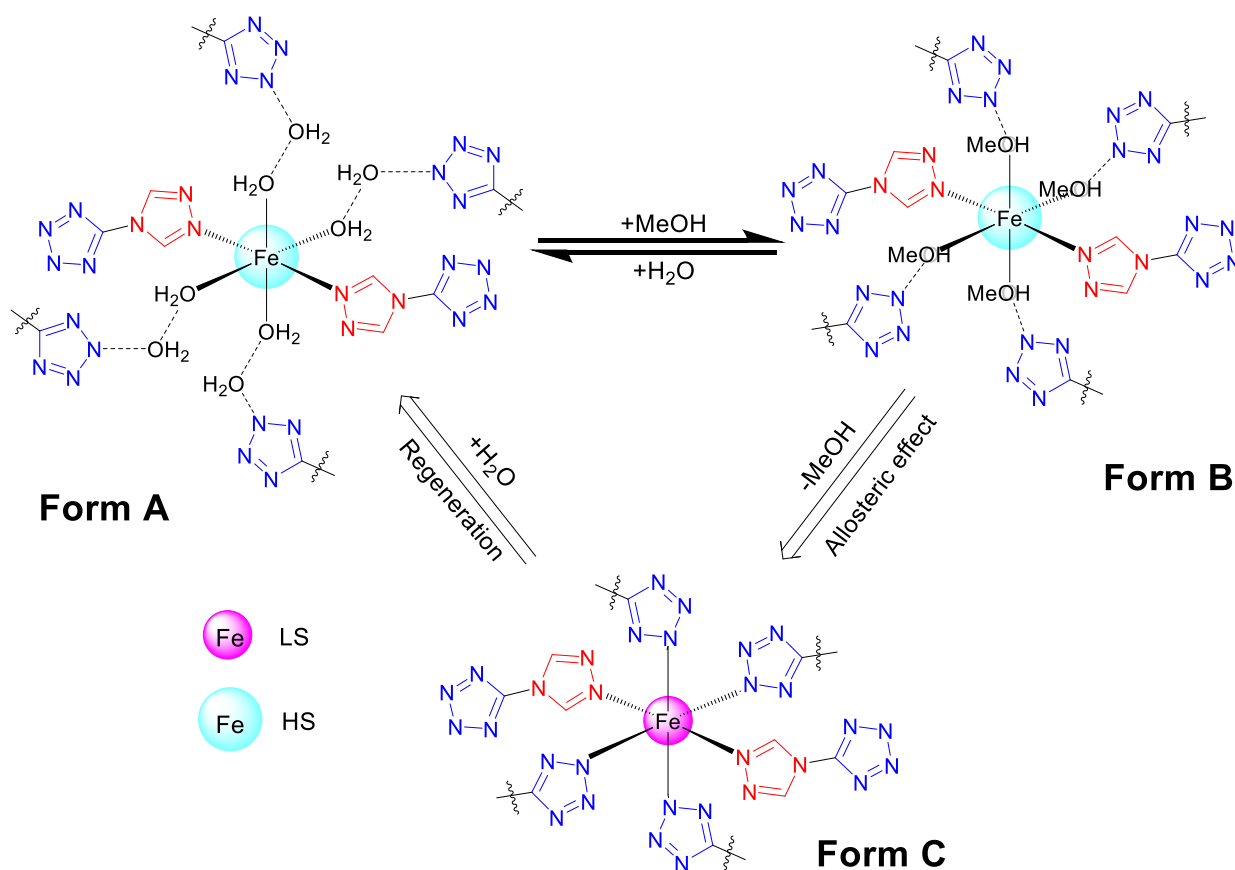
^a Crystal field splitting energy Δ was determined by the data of UV-vis spectrum as shown in ESI; ^b Tetragonal distortion (ε) were calculated based on $\Delta E_Q(T)$ data as shown in ESI in detail; ^c ref³⁴

HS1 and HS2 displays nearly identical isomer shifts ($\delta = 1.10$ and 1.04 mm/s) but distinctly different quadrupole splitting values ($\Delta E_Q = 2.95, 2.37$ mm/s), indicating different chemical distortions about iron centres. In Fe^{II} HS systems, a large quadrupole splitting reflects that the d^6 configuration with low electric field gradient (EFG) at the nucleus is splitted by a distortion to produce a high EFG situation. In **Fe-w5**, this distortion is attributed to imbalance t_{2g} orbitals of O_h symmetry, splitted by Jahn-Teller effect, leading to a D_{4h} field considering FeN_2O_4 environment, with a tetragonal compression energy (ε), as shown in Figure S

12. To estimate this effect, the relation between ΔE_Q and temperature can be applied by adapting the methods in reference:³⁵

$$\Delta E_Q = \frac{1}{2} eQ(V_{zz})_{(CF)} \propto \frac{1 - \exp\left(\frac{-\varepsilon}{k_B T}\right)}{1 + 2 \exp\left(\frac{-\varepsilon}{k_B T}\right)}$$

where eQ is the electric quadrupole moment of the 14.4-keV state of ^{57}Fe . The magnitude of ε was determined by computations based on $\Delta E_Q(T)$ data of Table 1 to the above equation, leading to 689 and 499 cm^{-1} for HS1 and HS2, respectively. This result demonstrates that substitution of coordinated water molecules by MeOH retains their HS, and merely releases the tetragonal compression to a certain extent. A full replace of FeN_6 , in contrast, would displays a neglecting ΔE_Q of 0.3mm/s, also reflecting vanished Jahn-Teller effect in d^6 -LS. Despite only 26% of the molecules undergoes spin-state switching, it is found higher compared to the prototype sensor in **Fe-w4** (22%).²² The persistent HS1 and HS2 sites are not due to crystallographic modifications that restrict further MeOH diffusion, but are attributed to the shortage of **trz-tet** ligands to compensate four position of each iron site for arousing FeN_6 sphere (*i.e.* Not every Fe^{II} can win around four tetrazole ligand for coordination).



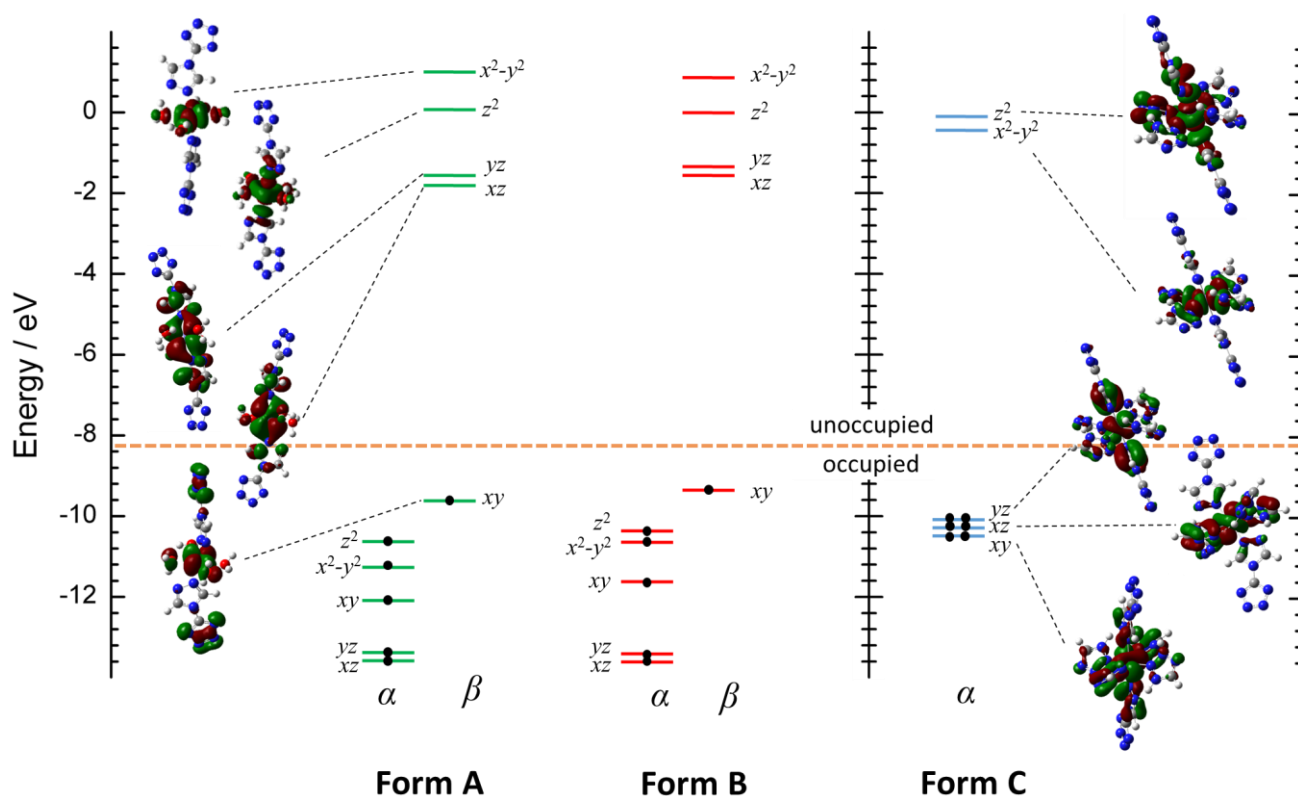


Figure 12. (top) Allosteric mechanism based on the sequence of colourimetric sensing and regeneration among forms **A**, **B** and **C**. (bottom) Energy level diagram and Fe *d*-based molecular orbitals of forms **A**, **B** and **C** (calculated at the CAM-B3LYP/6BS1 level of theory, for details see methodology in Section 5 of ESI).

4.3. Density Functional Calculations

A comparison of the ground state parameters (Table 2) shows good agreement between experimental data and the calculated parameters. The Fe-O/N bond lengths in form **A** and **B** are slightly higher than the X-ray structures in **Fe-w5**. This difference originates the temperature effect of crystal structure causing the slight contraction of bond length at 150 K. It does not affect the judgment $S = 2$ for both forms **A** and **B**. In contrast, form **C** has a $S = 0$ ground state with clearly shorter $r(\text{Fe-N})$ than forms **A** and **B**. Figure 12 shows the spin unrestricted energy level diagrams and relevant molecular orbitals.

Table 2. Comparison of experimental and computational gs parameters for forms **A**, **B** and **C**^a.

	Fe-w5 ^b	A ^c	B ^c	C ^c
$r(\text{Fe-O})$	2.081(6)-2.138(7)	2.191, 2.258	2.153, 2.234	-
$r(\text{Fe-N})$	2.174(9)-2.185(8)	2,100	2,101	1.950-1.995

^a All bond lengths are in Å. ^b from crystal structure of **Fe-w5** at 150 K. ^c Computational results calculated at the CAM-B3LYP/BS1 level of theory (for details see Table S 4).

Table 3. Spectroscopic assignments for **Fe-w5** before and after MeOH exchange. Comparison of experimental and computational transition energies (in nm) of forms **A**, **B** and **C**. (for details see Table S 5).

bands	<i>d-d</i> transitions	experimental (DRS)			computational (TD-DFT) ^a		
		A	B	C	A	B	C

I	$xy \rightarrow z^2/x^2-y^2$	~983	~972	-	701/841	694/806	-
II	$xy/xz/yz \rightarrow x^2-y^2$	-	-	~515	-	-	520/515/499
III	$xz/yz/xy \rightarrow z^2$	-	-	~361	-	-	364/356/322

In addition to the ground state parameters, we have calculated excited-state parameters to compare to spectroscopy. We use TD-DFT as implemented in Gaussian, to calculate energies of the electronic transitions in the ligand field. A comparison of the transition energies shows reasonable qualitative agreement between the experimental values (obtained by DRS spectroscopy) and the ones calculated by DFT (Table 3 and Section 5 in ESI). Forms **A** and **B** have similar transition energies. The calculations are consistent with the experimental assignment that band **I** is associated with the ligand field transition of an electron from the $d(xy)$ orbital into the $d(x^2-y^2)$ and $d(z^2)$ orbitals. In the calculated from **C**, the transition energies are associated with the ligand field band **II** and **III**, the $d(xy/xz/yz) \rightarrow d(x^2-y^2)$ and $d(xz/yz/xy) \rightarrow d(z^2)$ transitions, and show two sets of excitations around $\lambda = 540$ nm and $\lambda = 380-310$ nm as observed in the experimental spectra causing pink colour.

4.4 Magnetic dilution

In view of non-switchable HS iron sites, magnetic dilution sample of **Fe_{0.23}Zn_{0.77}-w5** was developed to explore the selectivity of analyte driving spin-state change.

Figure S13a-c presents a 10 μm wide of **Fe_{0.23}Zn_{0.77}-w5** needle crystal of SEM image with elemental maps of Zn and Fe, suggesting a homogeneous distribution. This provides convincing and compelling evidence of the formation of a magnetic dilution in solid state at the molecular scale, which is consistent with the observation from the PXRD of **Fe_{0.23}Zn_{0.77}-w5** in Figure S14. Inductive Coupled Plasma (ICP) was used to analyse quantitatively the atomic ratio. Zn and Fe were found to have relative contents of 77% and 23%, respectively.

The Mössbauer spectrum of **Fe_{0.23}Zn_{0.77}-w5** after sensing with MeOH is significantly changed as compared to **Fe-w5** in Figure 13. This shows an augmented quadrupole doublet (30%) with the same characteristics ($\delta = 0.38$ mm s⁻¹) as LS FeN₆ species, while the spectral area of HS1 had decreased from 43% to 39%. The observations suggest that allosteric effect preferential selected Fe^{II} site to arouse the LS state, probably because of the distinctive contraction from Fe^{II}-N₆ coordinated environment. It is well known that larger diluent ions like Zn^{II}, Co^{II} and Mn^{II} tend to exert a negative pressure on the Fe^{II} lattice, which stabilizes the HS form of a given spin crossover material.³⁶ In contrast, a correlation between metal-dilution and the promotion of LS state by allosteric effect in **Fe_{0.23}Zn_{0.77}-w5** demonstrates that another conversion mechanism is enabled, which makes disfavoured stabilization of LS, as a realistic scenario.

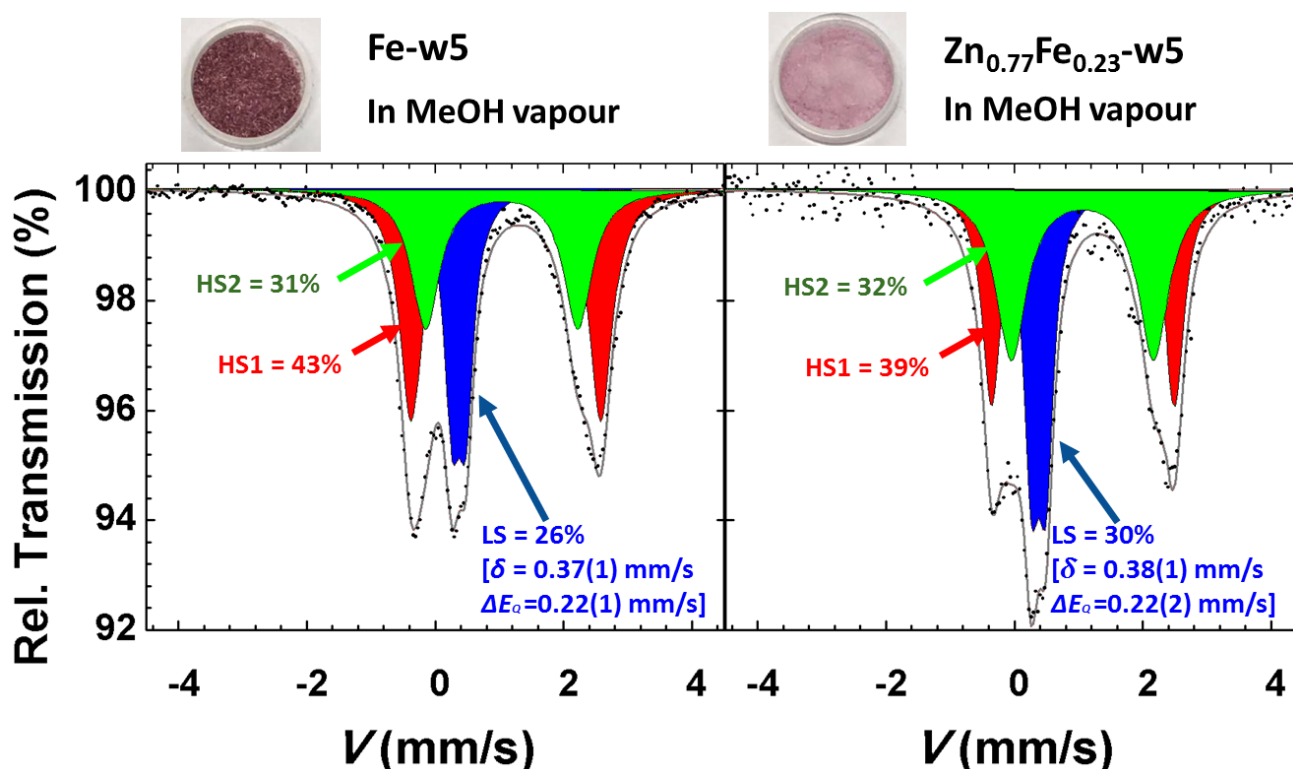


Figure 13. Room temperature ^{57}Fe Mössbauer spectra of **Fe-w5** (left) and **Fe_{0.23}Zn_{0.77}-w5** (right) after MeOH diffusion 10 h.

5. Conclusions

Fe-w4 and **Fe-w5** represent a new class of self-assembled supramolecular frameworks that possess periodicity and potential guest channel, in which common and versatile interstitial water is capable of directing the formation of pillared-layer architecture *via* supramolecular tessellations with rare **kgd** topology, further enabling Fe^{II} molecular building block as the function of chemical sensors. In contrast, **Fe-w0** without interstitial water cannot operate as a sensor material because of the tight crystal packing restricting any guest intrusion.

Despite SFs undergoes structure collapse to amorphous upon guest intrusion, it still exhibits a robust performance of reversible and bidirectional colourimetric sensing.³¹ The analyte driving spin-state change has been monitored and quantified by ^{57}Fe Mössbauer spectroscopy, NMR, DFT and magnetic dilution, and this accords fully with the proposed stepwise allosteric mechanism between HS FeN_2O_4 and LS FeN_6 chromophore.

Therefore, this finding provides fascinating opportunities for creating multifunctional SF based on simple but constructional supramolecular tiling, demonstrating the feasibility of the emerging SFs for their potential applications. Especially, the synthesis of supramolecular frameworks with the edge-transitive **kgd** topology is considered important also because these solids could serve as blueprints for the development of novel pillared SFs with targeted pore characteristics and functionalities.

6 Experimental

All the chemicals were bought from usual chemical companies and used as received without further purification. **trz-tetH** ligand and crystalline sample of **Fe-w4** was prepared according to our previous method.²² All the experiment was carried out in air without inert atmosphere protection.

[Fe(trz-tet)₂(H₂O)₄]·5H₂O (Fe-w5). trz-tetH (100 mg, 0.72 mmol, 3 equiv.) was dissolved in water (10 mL) by warming to 60°C. Fe(ClO₄)₂·6H₂O (82.06 mg, 0.24 mmol, 1 equiv.) was added to the above solution of trz-tetH. The resulting clear solution (pH ≈ 1) was stirred for 20 min. at 60°C and then quenched in an ice bath overnight. Large amount needle crystals were obtained under low temperature. Yield: 25 mg (82%). TGA for fresh sample: 5H₂O, 18.37%; Found, 18.73%. Anal. Calcd. (%) for air-dried sample C₆H₁₂FeN₁₄O₄: C, 18.01; H, 3.02; N, 49.01. Found: C, 18.20; H, 4.20; N, 48.23.

[Fe(trz-tet)₂(H₂O)₄] (Fe-w0). Crystals **Fe-w0** were obtained as a by-product during the crystallization **Fe-w4**²² by slowly evaporate the solution at room temperature for more than three days as hard parallelogram crystals. The molecular structure of these tiny crystals corresponds exactly to **Fe-w0**.

[Fe_{0.23}Zn_{0.77}(trz-tet)₂(H₂O)₄]·5H₂O (Fe_{0.23}Zn_{0.77}-w5). The diluted compound **Fe_{0.23}Zn_{0.77}-w5** was synthesized according to the same procedure with **Fe-w5**, replacing the metal salt by mixtures of 25% equiv. Fe(ClO₄)₂·6H₂O and 75% equiv Zn(ClO₄)₂·6H₂O. ICP test provided the chemical composition of Fe:Zn = 0.23:0.77. EDX shown in Figure S 13. The PXRD of **Fe-w5** and diluted **Fe_{0.23}Zn_{0.77}-w5** have been recorded and both compounds are isomorphous. (Figure S 14).

Physical measurements and single crystal X-ray analyses **were shown in ESI**

Conflicts of interest

There are no conflicts to declare.

Acknowledgements

This research was supported by FNRS fellowships of chargé de Recherches (28109061 and 24918505); the initial founding of Zhejiang Sci-Tech University (11432932611902 and 11432932612014) and FNRS (CDR 33694457, PDR T.0095.21). We thank Dr. He Jia (UCLouvain) for the help of the measurement of SEM and discussion. J. O. thanks the financial support of 2018-1.2.1-NKP-2018-00005 of the National Research, Development and Innovation Fund of Hungary, of CELSA/19/017. Useful discussions with Z. Benkó, J.N. Harvey and T. Veszprémi are also acknowledged.

Supporting Information

Instrumentation, crystallographic information, optical sensing and crystal field analyses as well as computational details are supplied as supporting information.

References

1. J. Tian, H. Wang, D.-W. Zhang, Y. Liu and Z.-T. Li, Supramolecular organic frameworks (SOFs): homogeneous regular 2D and 3D pores in water, *Natl. Sci. Rev.*, 2017, **4**, 426-436.
2. S. Mehrparvar, C. Wölper, R. Gleiter and G. Haberhauer, The Carbonyl···Tellurazole Chalcogen Bond as a Molecular Recognition Unit: From Model Studies to Supramolecular Organic Frameworks, *Angew. Chem., Int. Ed.*, **59**, 17154-17161.
3. N. Yoshinari, N. Meundaeng, H. Tabe, Y. Yamada, S. Yamashita, Y. Nakazawa and T. Konno, Single-Crystal-to-Single-Crystal Installation of Ln₄(OH)₄ Cubanes in an Anionic Metallosupramolecular Framework, *Angew. Chem., Int. Ed.*, 2020, **59**, 18048-18053.
4. J. Wu, M. Guo, X.-L. Li, L. Zhao, Q.-F. Sun, R. A. Layfield and J. Tang, From double-shelled grids to supramolecular frameworks, *Chem. Commun.*, 2018, **54**, 12097-12100.

5. J. Tian, Z.-Y. Xu, D.-W. Zhang, H. Wang, S.-H. Xie, D.-W. Xu, Y.-H. Ren, H. Wang, Y. Liu and Z.-T. Li, Supramolecular metal-organic frameworks that display high homogeneous and heterogeneous photocatalytic activity for H₂ production, *Nat. Commun.*, 2016, **7**, 11580.
6. J. Dai, D. Xie, Y. Liu, Z. Zhang, Y. Yang, Q. Yang, Q. Ren and Z. Bao, Supramolecular Metal–Organic Framework for CO₂/CH₄ and CO₂/N₂ Separation, *Ind. Eng. Chem. Res.*, 2020, **59**, 7866-7874.
7. J.-H. Deng, J. Luo, Y.-L. Mao, S. Lai, Y.-N. Gong, D.-C. Zhong and T.-B. Lu, π - π stacking interactions: Non-negligible forces for stabilizing porous supramolecular frameworks, *Sci. Adv.*, 2020, **6**, eaax9976.
8. X.-L. Luo, Z. Yin, M.-H. Zeng and M. Kurmoo, The construction, structures, and functions of pillared layer metal–organic frameworks, *Inorg. Chem. Front.*, 2016, **3**, 1208-1226.
9. L. Liu, Z. Yao, Y. Ye, Y. Yang, Q. Lin, Z. Zhang, M. O’Keeffe and S. Xiang, Integrating the Pillared-Layer Strategy and Pore-Space Partition Method to Construct Multicomponent MOFs for C₂H₂/CO₂ Separation, *J. Am. Chem. Soc.*, 2020, **142**, 9258-9266.
10. V. Guillerm, D. Kim, J. F. Eubank, R. Luebke, X. Liu, K. Adil, M. S. Lah and M. Eddaoudi, A supermolecular building approach for the design and construction of metal–organic frameworks, *Chem. Soc. Rev.*, 2014, **43**, 6141-6172.
11. B. Grünbaum and G. C. Shephard, *Tilings and Patterns*, W. H. Freeman and Company, 1987.
12. D. Eppstein, Diamond-kite adaptive quadrilateral meshing, *Eng. Comput.*, 2013, **30**, 223-235.
13. I. Spanopoulos, C. Tsangarakis, S. Barnett, H. Nowell, E. Klontzas, G. E. Froudakis and P. N. Trikalitis, Directed assembly of a high surface area 2D metal–organic framework displaying the augmented “kagomé dual” (kgd-a) layered topology with high H₂ and CO₂ uptake, *Inorg. Chem. Front.*, 2017, **4**, 825-832.
14. Y.-Q. Zhang, M. Paszkiewicz, P. Du, L. Zhang, T. Lin, Z. Chen, S. Klyatskaya, M. Ruben, A. P. Seitsonen, J. V. Barth and F. Klappenberger, Complex supramolecular interfacial tessellation through convergent multi-step reaction of a dissymmetric simple organic precursor, *Nat. Chem.*, 2018, **10**, 296-304.
15. F. Cheng, X.-J. Wu, Z. Hu, X. Lu, Z. Ding, Y. Shao, H. Xu, W. Ji, J. Wu and K. P. Loh, Two-dimensional tessellation by molecular tiles constructed from halogen–halogen and halogen–metal networks, *Nat. Commun.*, 2018, **9**, 4871.
16. D. Écija, J. I. Urgel, A. C. Papageorgiou, S. Joshi, W. Auwärter, A. P. Seitsonen, S. Klyatskaya, M. Ruben, S. Fischer, S. Vijayaraghavan, J. Reichert and J. V. Barth, Five-vertex Archimedean surface tessellation by lanthanide-directed molecular self-assembly, *Proc. Natl. Acad. Sci.*, 2013, **110**, 6678-6681.
17. C. Lu, Y. Li, L.-M. Wang, H.-J. Yan, L. Chen and D. Wang, Rational design of two-dimensional covalent tilings using a C₆-symmetric building block via on-surface Schiff base reaction, *Chem. Commun.*, 2019, **55**, 1326-1329.
18. S.-i. Ohkoshi, Y. Tsunobuchi, H. Takahashi, T. Hozumi, M. Shiro and K. Hashimoto, Synthesis and Alcohol Vapor Sensitivity of a Ferromagnetic Copper–Tungsten Bimetallic Assembly, *J. Am. Chem. Soc.*, 2007, **129**, 3084-3085.
19. S.-i. Ohkoshi, K. Imoto, Y. Tsunobuchi, S. Takano and H. Tokoro, Light-induced spin-crossover magnet, *Nat. Chem.*, 2011, **3**, 564-569.
20. S.-i. Ohkoshi, K.-i. Arai, Y. Sato and K. Hashimoto, Humidity-induced magnetization and magnetic pole inversion in a cyano-bridged metal assembly, *Nat. Mater.*, 2004, **3**, 857-861.
21. S.-i. Ohkoshi, S. Takano, K. Imoto, M. Yoshikiyo, A. Namai and H. Tokoro, 90-degree optical switching of output second-harmonic light in chiral photomagnet, *Nat. Photonics*, 2014, **8**, 65-71.
22. A. D. Naik, K. Robeyns, C. F. Meunier, A. F. Léonard, A. Rotaru, B. Tinant, Y. Filinchuk, B. L. Su and Y. Garcia, Selective and Reusable Iron(II)-Based Molecular Sensor for the Vapor-Phase Detection of Alcohols, *Inorg. Chem.*, 2014, **53**, 1263-1265.
23. R. Wang, Z. Wang, Y. Xu, F. Dai, L. Zhang and D. Sun, Porous Zirconium Metal–Organic Framework Constructed from 2D \rightarrow 3D Interpenetration Based on a 3,6-Connected kgd Net, *Inorg. Chem.*, 2014, **53**, 7086-7088.
24. M. Li, B. Hua, H. Liang, J. Liu, L. Shao and F. Huang, Supramolecular Tessellations via Pillar[n]arenes-Based Exo–Wall Interactions, *J. Am. Chem. Soc.*, 2020, **142**, 20892-20901.
25. H. Jiang, W. Zhang, X. Kang, Z. Cao, X. Chen, Y. Liu and Y. Cui, Topology-Based Functionalization of Robust Chiral Zr-Based Metal–Organic Frameworks for Catalytic Enantioselective Hydrogenation, *J. Am. Chem. Soc.*, 2020, **142**, 9642-9652.

26. F. Hu, Z. Di, M. Wu and J. Li, Building a robust 3D Ca-MOF by a new square Ca₄O SBU for purification of natural gas, *Dalton Trans.*, 2020, **49**, 8836-8840.
27. W.-J. Shi, Y.-Z. Li, Q.-X. Hu, G.-D. Wang, L. Hou and Y.-Y. Wang, New scu topological MOF based on azolyl-carboxyl bifunctional linker: Gas adsorption and luminescence properties, *J. Solid State Chem.*, 2020, **283**, 121170.
28. J.-M. Liu, J.-X. Hou, J. Liu, X. Jing, L.-J. Li and J.-L. Du, Pyrazinyl-functionalized Zr(IV)-MOF for ultrasensitive detection of tyrosine/TNP and efficient CO₂/N₂ separation, *J. Mater. Chem. C*, 2019, **7**, 11851-11857.
29. J. Lyu, X. Zhang, K.-i. Otake, X. Wang, P. Li, Z. Li, Z. Chen, Y. Zhang, M. C. Wasson, Y. Yang, P. Bai, X. Guo, T. Islamoglu and O. K. Farha, Topology and porosity control of metal–organic frameworks through linker functionalization, *Chem. Sci.*, 2019, **10**, 1186-1192.
30. W. Gong, X. Chen, H. Jiang, D. Chu, Y. Cui and Y. Liu, Highly Stable Zr(IV)-Based Metal–Organic Frameworks with Chiral Phosphoric Acids for Catalytic Asymmetric Tandem Reactions, *J. Am. Chem. Soc.*, 2019, **141**, 7498-7508.
31. Y. Guo, S. Xue, M. M. Dîrtu and Y. Garcia, A versatile iron(ii)-based colourimetric sensor for the vapor-phase detection of alcohols and toxic gases, *J. Mater. Chem. C*, 2018, **6**, 3895-3900.
32. C.-F. Wang, M.-J. Sun, Q.-J. Guo, Z.-X. Cao, L.-S. Zheng and J. Tao, Multiple correlations between spin crossover and fluorescence in a dinuclear compound, *Chem. Commun.*, 2016, **52**, 14322-14325.
33. A. R. Riordan, A. Jansma, S. Fleischman, D. B. Green and D. R. Mulford, Spectrochemical Series of Cobalt(III), *Chem. Educat.*, 2005, **10**, 115-119.
34. A. D. Naik, A. P. Railliet, M. M. Dîrtu and Y. Garcia, Coordination preference and magnetic properties of FeII assemblies with a bis-azole bearing 1,2,4-triazole and tetrazole, *Hyperfine Interact.*, 2012, **204**, 119-123.
35. P. R. Edwards, C. E. Johnson and R. J. P. Williams, Mössbauer Spectra of Some Tetrahedral Iron (II) Compounds, *J. Chem. Phys.*, 1967, **47**, 2074-2082.
36. C. A. Tovee, C. A. Kilner, J. A. Thomas and M. A. Halcrow, Co-crystallising two functional complex molecules in a terpyridine embrace lattice, *CrystEngComm*, 2009, **11**, 2069-2077.